

Electronic Supplementary Information (ESI)

Multiphoton ultraviolet upconversion through selectively controllable energy transfer in confined sensitizing sublattice towards improved solar photocatalysis

Songbin Liu,¹ Jinshu Huang,¹ Long Yan,¹ Nan Song,¹ Peng Zhang,¹ Junshan He,¹ and Bo Zhou^{1,}*

¹ State Key Laboratory of Luminescent Materials and Devices, Guangdong Provincial Key Laboratory of Fiber Laser Materials and Applied Techniques, Guangdong Engineering Technology Research and Development Center of Special Optical Fiber Materials and Devices, South China University of Technology, Guangzhou 510641, China

***Corresponding author:**

E-mail: (B.Z.) zhoubo@scut.edu.cn

Figure S1~24

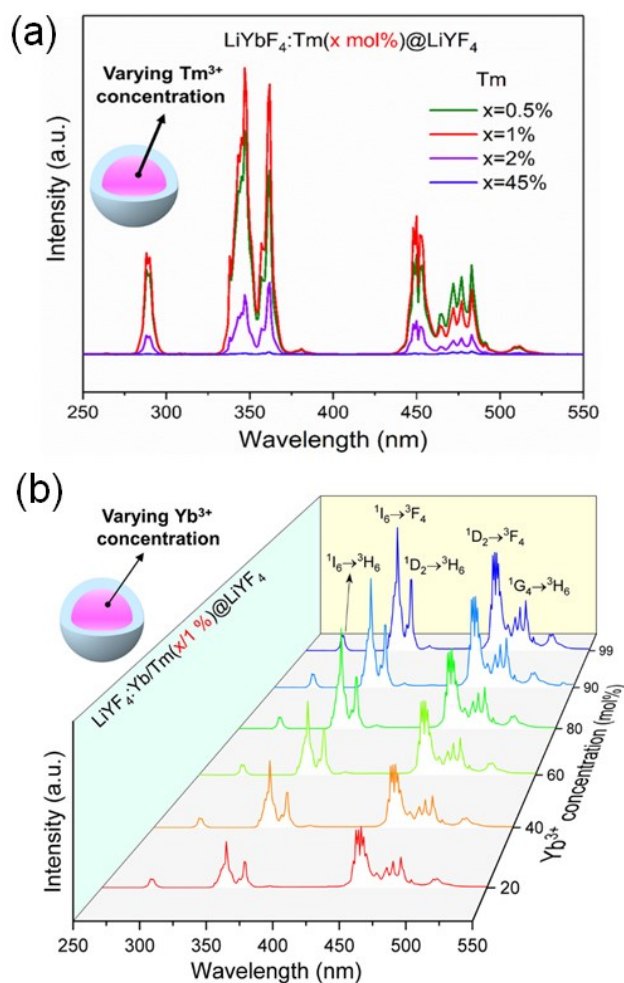


Figure S1. (a) Upconversion emission spectra of LiYbF₄:Tm(x mol%)@LiYF₄ core-shell nanoparticles (x = 0.5, 1, 2, 4 mol%) with different Tm³⁺ doping concentrations in the core region under 980 nm NIR excitation. (b) Upconversion emission spectra of LiYF₄:Yb/Tm(x/1 mol%)@LiYF₄ core-shell nanoparticles (x = 20, 40, 60, 80, 99 mol%) with different Yb³⁺ doping concentrations in the core under 980 nm NIR excitation.

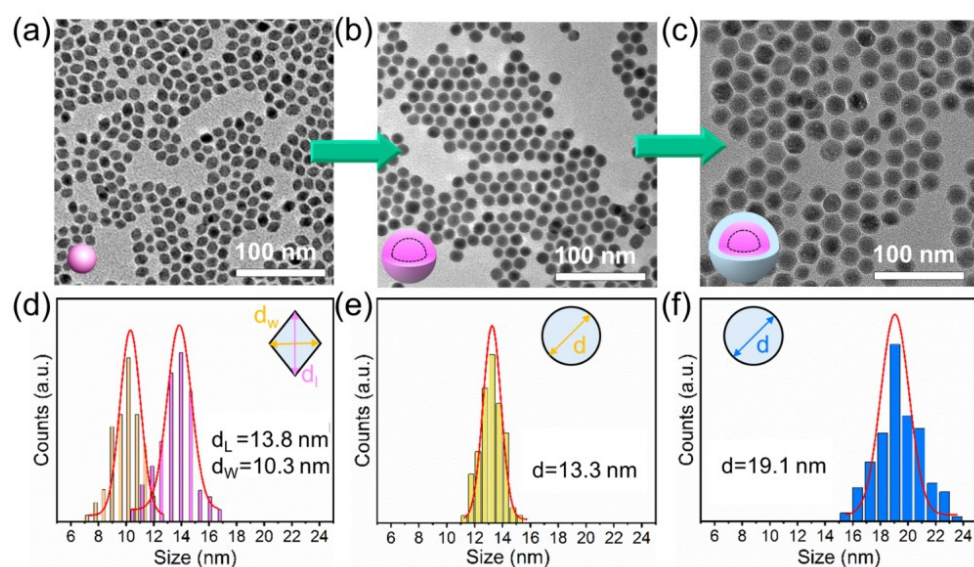


Figure S2. TEM images and corresponding size distributions of as-synthesized nanoparticles. (a,d) $\text{LiYbF}_4\text{:Tm}(1 \text{ mol}\%)$ initial nuclei; (b,e) $\text{LiYbF}_4\text{:Tm}(1 \text{ mol}\%)\text{-LiYbF}_4$ core; (c,f) $\text{LiYbF}_4\text{:Tm}(1 \text{ mol}\%)\text{-LiYbF}_4\text{@LiYF}_4$ core-shell sample. Note that the histograms of size distribution were obtained by calculating more than 250 particles from the TEM image.

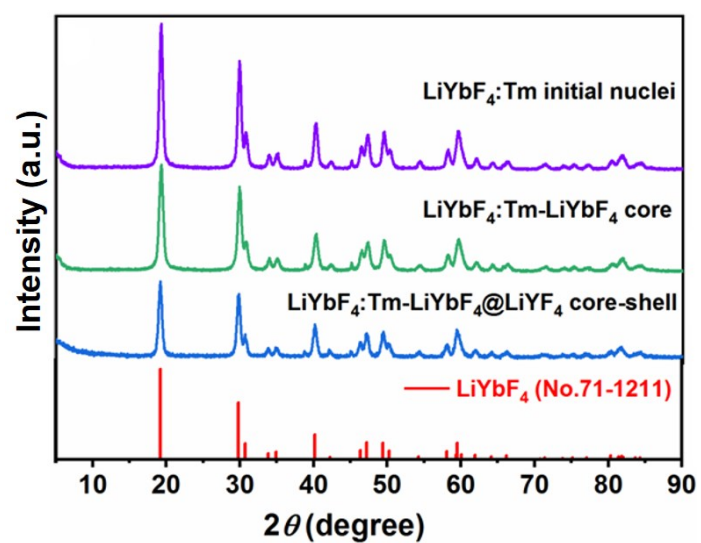


Figure S3. XRD patterns of initial nuclei, core, and core-shell for LiYbF₄:Tm(1 mol%)-LiYbF₄@LiYF₄ nanoparticles, respectively. Note that the standard JCPDS data for tetragonal-phased LiYbF₄ (PDF #71-1211) was also presented.

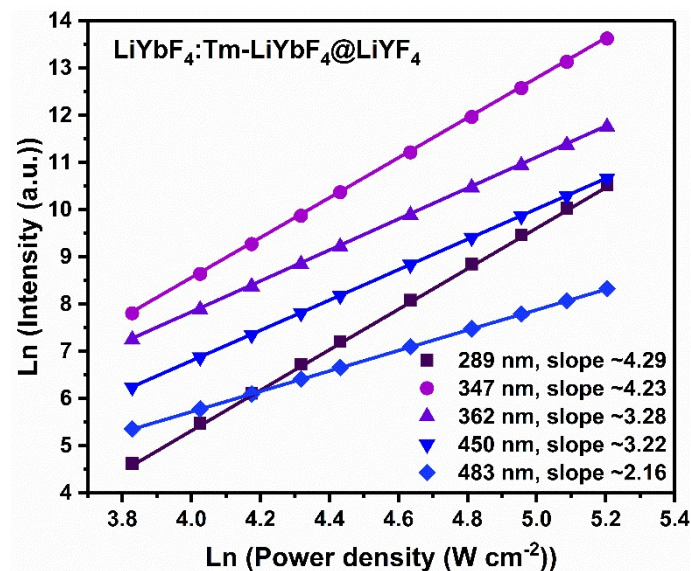


Figure S4. Power density dependence of the Tm^{3+} emissions at 289 nm ($^1\text{I}_6 \rightarrow ^3\text{H}_6$), 347 nm ($^1\text{I}_6 \rightarrow ^3\text{F}_4$), 362 nm ($^1\text{D}_2 \rightarrow ^3\text{H}_6$), 450 nm ($^1\text{D}_2 \rightarrow ^3\text{F}_4$), and 483 nm ($^1\text{G}_4 \rightarrow ^3\text{H}_6$) for $\text{LiYbF}_4:\text{Tm}(1 \text{ mol}\%)-\text{LiYbF}_4@\text{LiYF}_4$ core-shell nanoparticles under 980 nm excitation. The log-log slope values of 4.29, 4.23, 3.28, 3.22, and 2.16 are in agreement with the 5-, 4- and 3-photon upconversion processes of the emissions from $^1\text{I}_6$, $^1\text{D}_2$, and $^1\text{G}_4$ levels of Tm^{3+} that yield the typical UV and blue emissions, respectively.

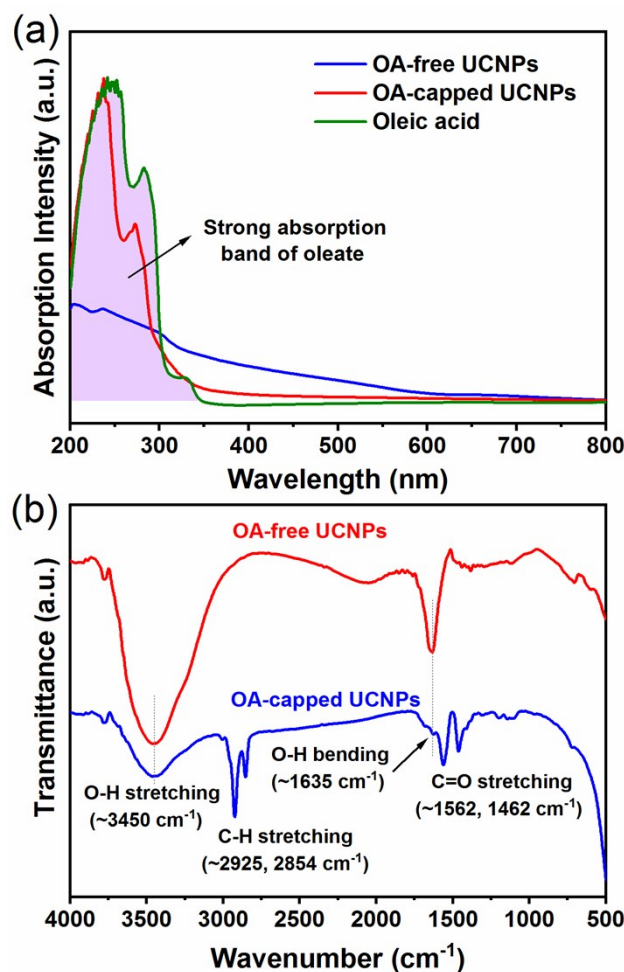


Figure S5. (a) Absorption spectra of oleic acid (OA), OA-capped LiYbF₄:Tm(1 mol%)-LiYbF₄@LiYF₄ core-shell UCNPs dispersed in cyclohexane solution, and OA-free UCNPs dispersed in deionized water. The strong absorption band of the oleate overlaps with the emission of Tm³⁺ in the UV spectral region, resulting in a relatively weak UV upconversion emission. (b) FT-IR spectra of OA-capped and OA-free LiYbF₄:Tm(1 mol%)-LiYbF₄@LiYF₄ core-shell UCNPs, respectively. The results reveal that the oleate-related absorption bands (C-H, C=O stretching) disappeared after washing the nanoparticles with HCl solution, confirming the successful removal of oleate ligands from the particle surface. Note that strong O-H absorption bands from the OA-free nanoparticles are due to water molecules physically absorbed on the particle surface.

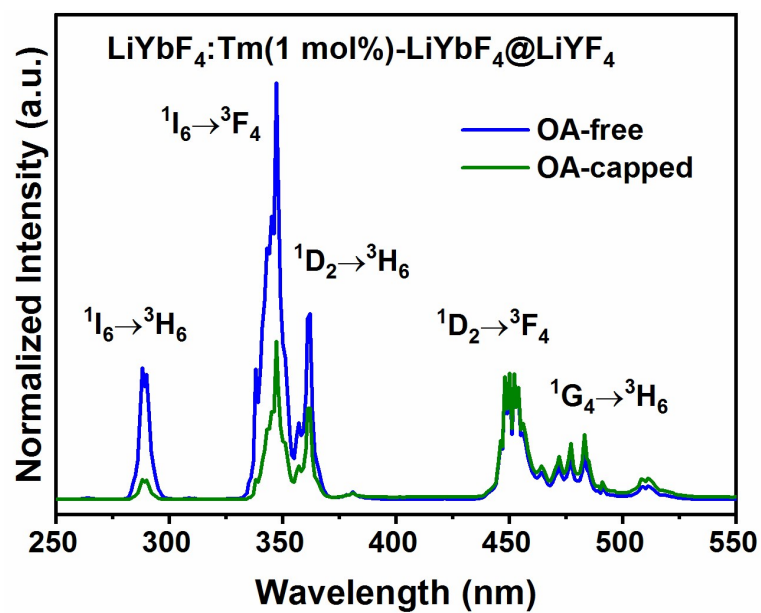


Figure S6. Upconversion emission spectra of OA-capped and OA-free LiYbF₄:Tm(1 mol%)-LiYbF₄@LiYF₄ core-shell UCNPs under 980 nm NIR excitation.

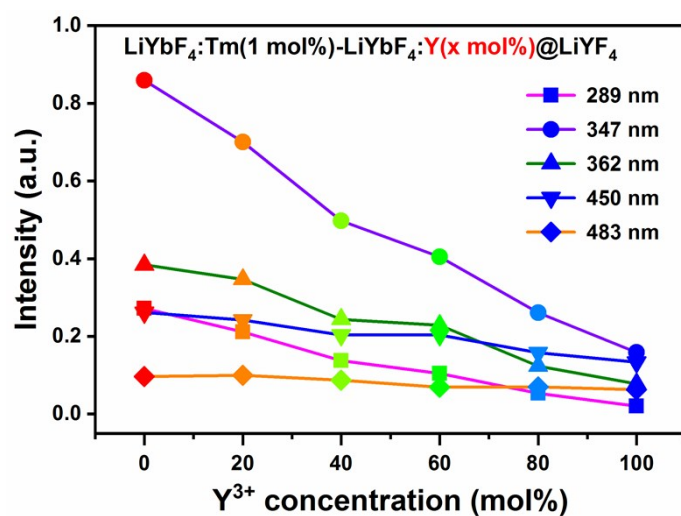


Figure S7. Upconversion emission intensity at 289, 347, 362, 450, 483 nm as a function of Y³⁺ doping concentrations in the margin region of the sensitizing core for the LiYbF₄:Tm(1 mol%)-LiYbF₄:Y(x; 0-100 mol%)@LiYF₄ core-shell- nanoparticles under 980 nm NIR excitation.

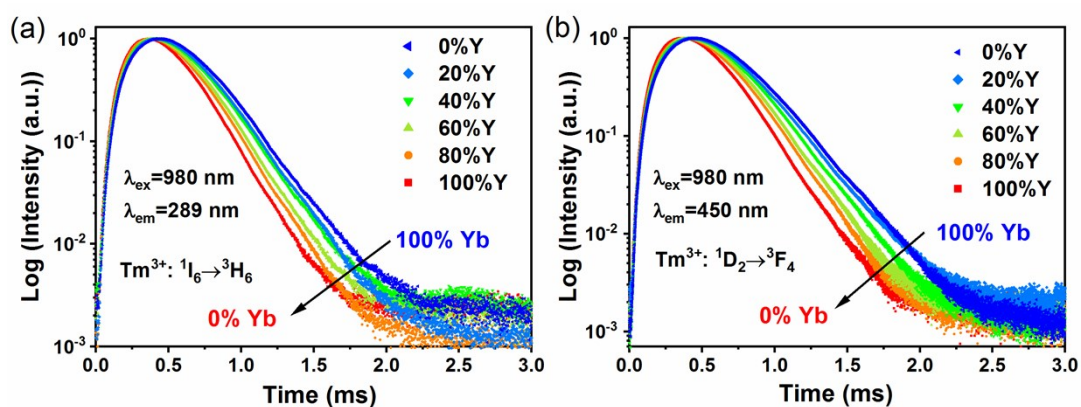


Figure S8. Decay curves obtained from the LiYbF₄:Tm(1 mol%)-LiYbF₄:Y (x; x=0-100 mol%)-LiYF₄ core-shell nanoparticles with various Yb³⁺ doping concentration in the margin region of the sensitizing core by monitoring corresponding emission wavelengths after excitation with a pulse laser at 980 nm. (a) Decay curves of Tm³⁺ emission at 289 nm (¹I₆→³H₆ transition). (b) Decay curves of Tm³⁺ emission at 450 nm (¹D₂→³F₄ transition).

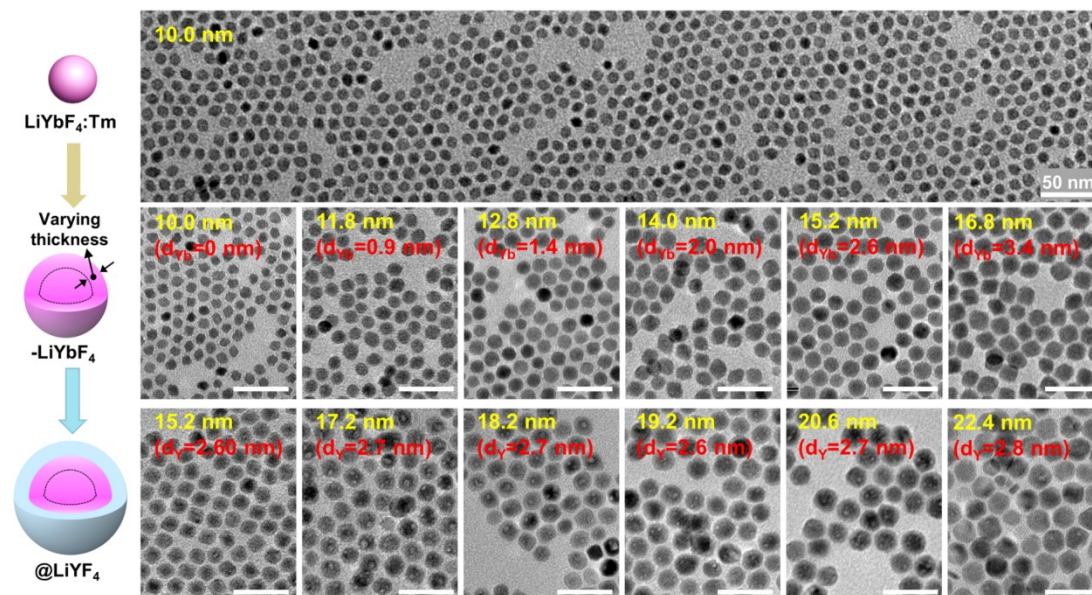


Figure S9. TEM images of the as-synthesized LiYbF₄:Tm(1 mol%)-LiYbF₄@LiYF₄ core-shell nanoparticles with varying LiYbF₄ thickness in margin region of the sensitizing core (0~3.4 nm). The initial nuclei particles with a diameter ~10.0 nm were synthesized and separated for following epitaxial shell growth for core and core-shell nanoparticles. Thickness of LiYbF₄ in margin region was tuned by adding the amount of precursors. Scale bars, 50 nm.

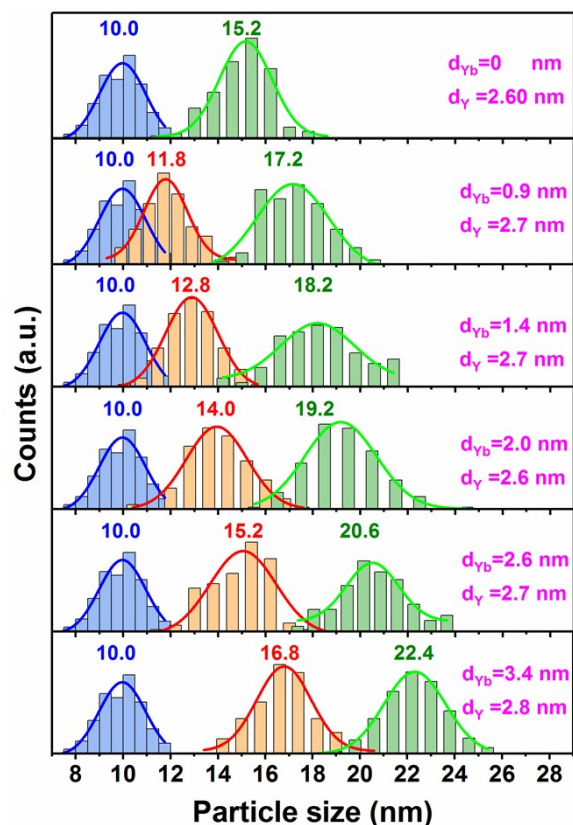


Figure S10. The size distributions of LiYbF₄:Tm(1 mol%)-LiYbF₄@LiYF₄ core-shell nanoparticles with varying LiYbF₄ thickness in margin region of the sensitizing core in Figure S9. Note that the histograms of size distributions were obtained by calculating more than 250 particles from the TEM images. The d_{Yb} and d_Y represents the thickness of LiYbF₄ margin region in sensitizing core and LiYF₄ inert-shell layer, respectively.

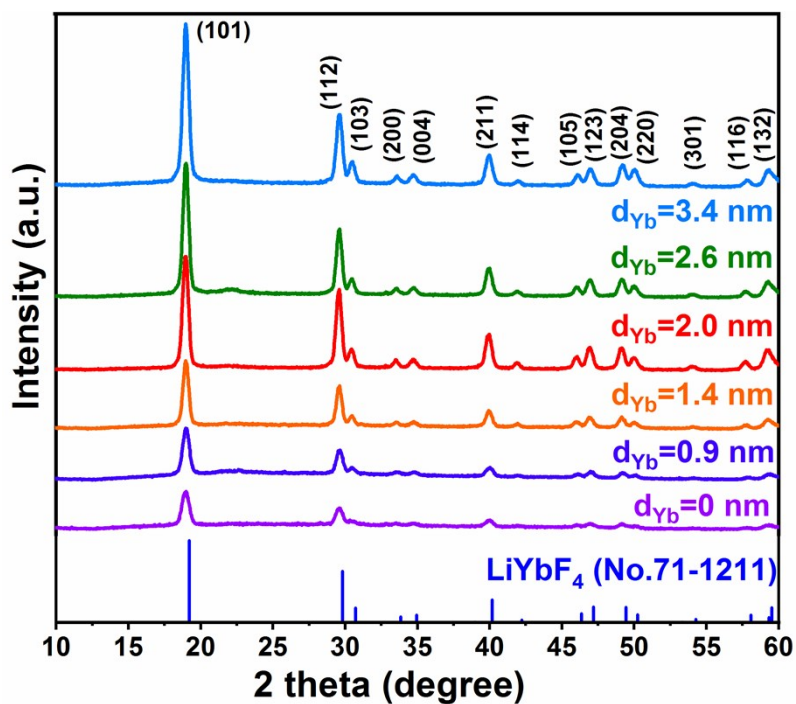


Figure S11. XRD patterns of the as-synthesized LiYbF₄:Tm(1 mol%)-LiYbF₄@LiYF₄ core-shell nanoparticles with varying LiYbF₄ thickness in margin region of the sensitizing core. Note that the standard JCPDS data for tetragonal-phased LiYbF₄ (PDF #71-1211) is also presented.

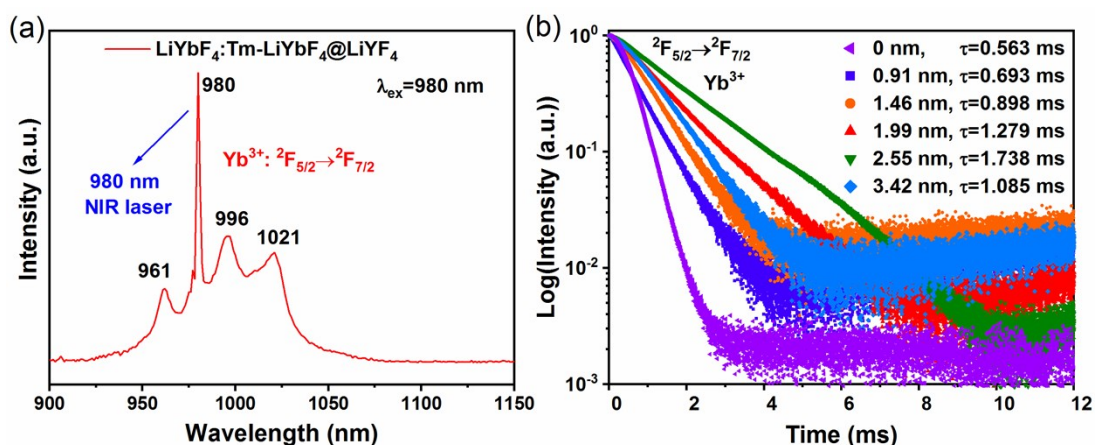


Figure S12. (a) NIR emission spectra obtained from LiYbF₄:Tm(1 mol%)-LiYbF₄@LiYF₄ core-shell nanoparticles under 980 nm excitation. Note that the emission slit of the spectrometer was kept very small to reduce the interference of 980 nm laser source signal. (b) Decay curves of ²F_{5/2} state of Yb³⁺ in the LiYbF₄:Tm(1 mol%)-LiYbF₄@LiYF₄ core-shell nanoparticles with varying thickness of LiYbF₄ margin region in sensitizing core by monitoring the emission at 1021 nm with a pulse laser at 980 nm.

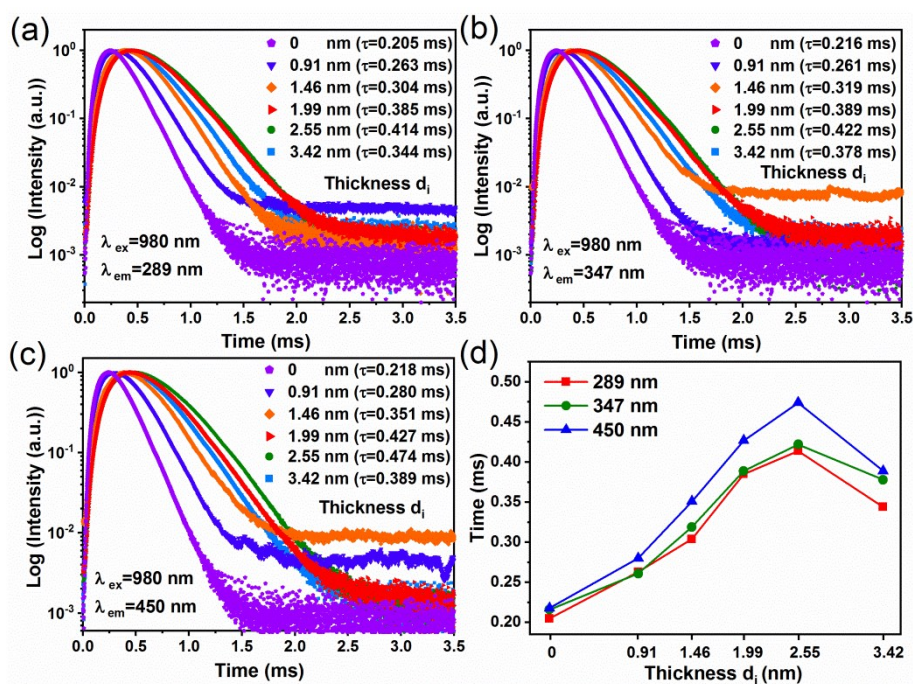


Figure S13. Decay curves of Tm^{3+} emission obtained from the $LiYbF_4:Tm(1 \text{ mol}\%)-LiYbF_4@LiYF_4$ core-shell nanoparticles with varying thickness of $LiYbF_4$ margin region in sensitizing core by monitoring corresponding emission wavelength with a pulse laser at 980 nm. (a) Tm^{3+} emission at 289 nm ($^1I_6 \rightarrow ^3H_6$ transition). (b) Tm^{3+} emission at 347 nm ($^1I_6 \rightarrow ^3F_4$ transition). (c) Tm^{3+} emission at 450 nm ($^1D_2 \rightarrow ^3F_4$ transition) (d) Lifetime of Tm^{3+} emission at 289, 347 and 450 nm as a function of $LiYbF_4$ thickness. Note that the corresponding calculated lifetime value were marked.

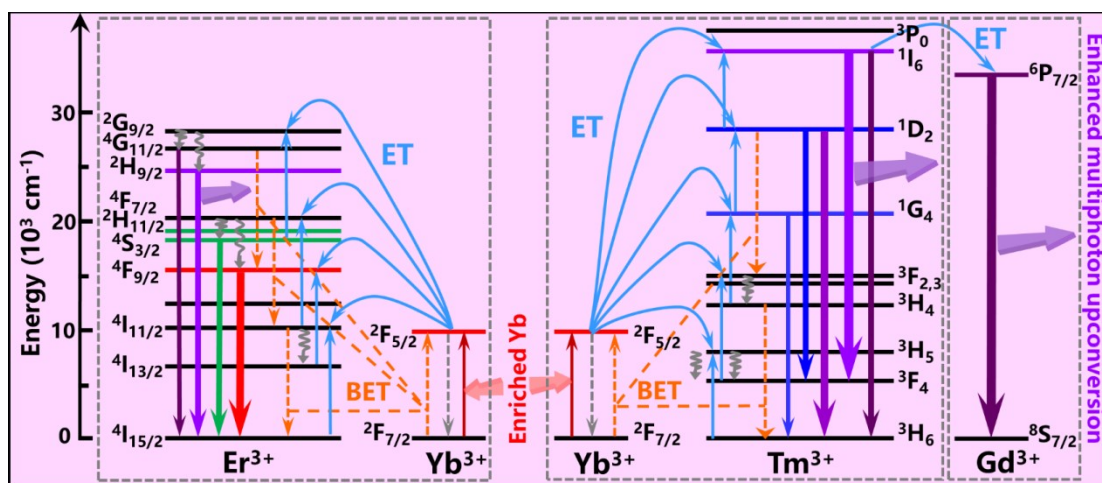


Figure S14. Simplified energy-level diagram and upconversion mechanism for enhanced multiphoton UV upconversion emission in Tm^{3+} , Er^{3+} , or Gd^{3+} -doped system.

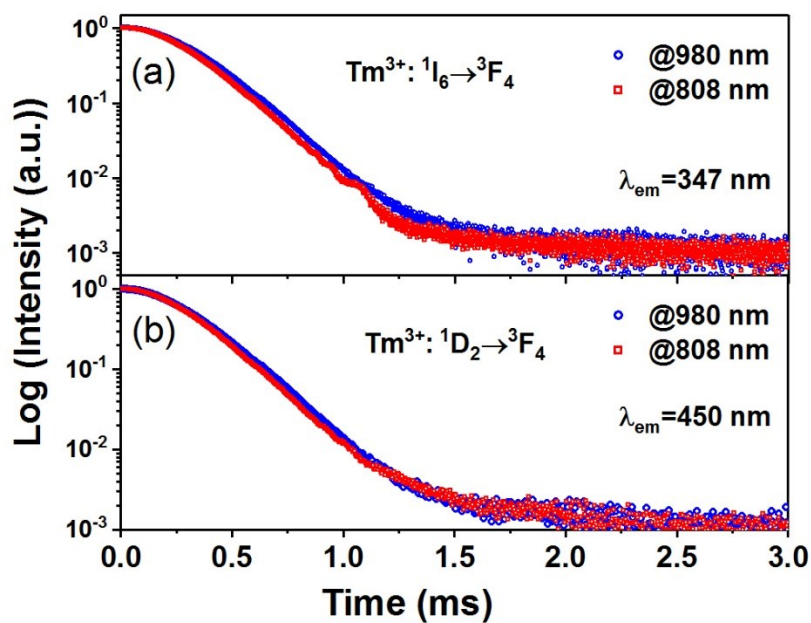


Figure S15. Decay curves of Tm^{3+} emission obtained from $\text{LiYbF}_4:\text{Tm}(1 \text{ mol}\%)-\text{LiYbF}_4@\text{LiYF}_4:\text{Nd}(40 \text{ mol}\%)$ core-shell nanoparticles at (a) 347 nm and (b) 450 nm under pulsed 980 and 808 dual-wavelength excitation.

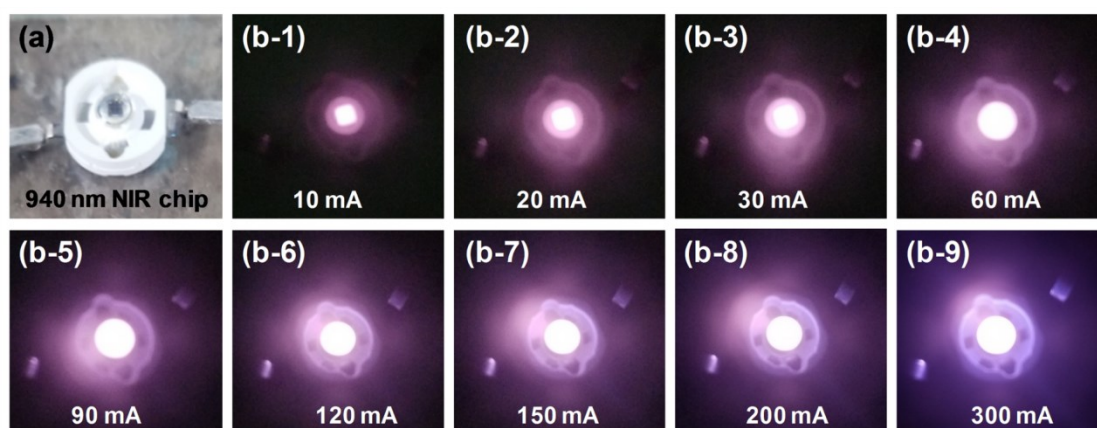


Figure S16. Digital images of packaged UV-emitting LED device combining with 940 nm NIR chip and as-synthesized $\text{LiYbF}_4:\text{Tm}(1 \text{ mol}\%)-\text{LiYbF}_4@\text{LiYF}_4$ core-shell nanoparticles operated at different forward bias currents. It shows the image (a) before applying the current and (b) after applying the current at 10, 20, 30, 60, 90, 120, 150, 200, and 300 mA, respectively.

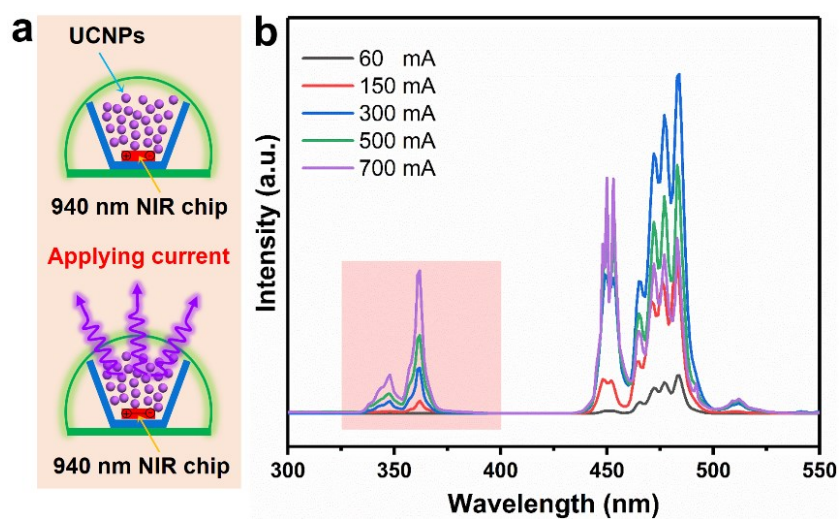


Figure S17. (a) Schematic illustration of UV-emitting LED fabrication by coating the UCNPs on the surface of a 940 nm NIR chip to emit UV upconversion emission under applying current. (b) Electroluminescence spectra of the fabricated LED device combined with 940 nm NIR chip and as-synthesized $\text{LiYbF}_4:\text{Tm}(1 \text{ mol}\%)-\text{LiYbF}_4@\text{LiYF}_4$ core-shell nanoparticles operated at different forward bias currents.

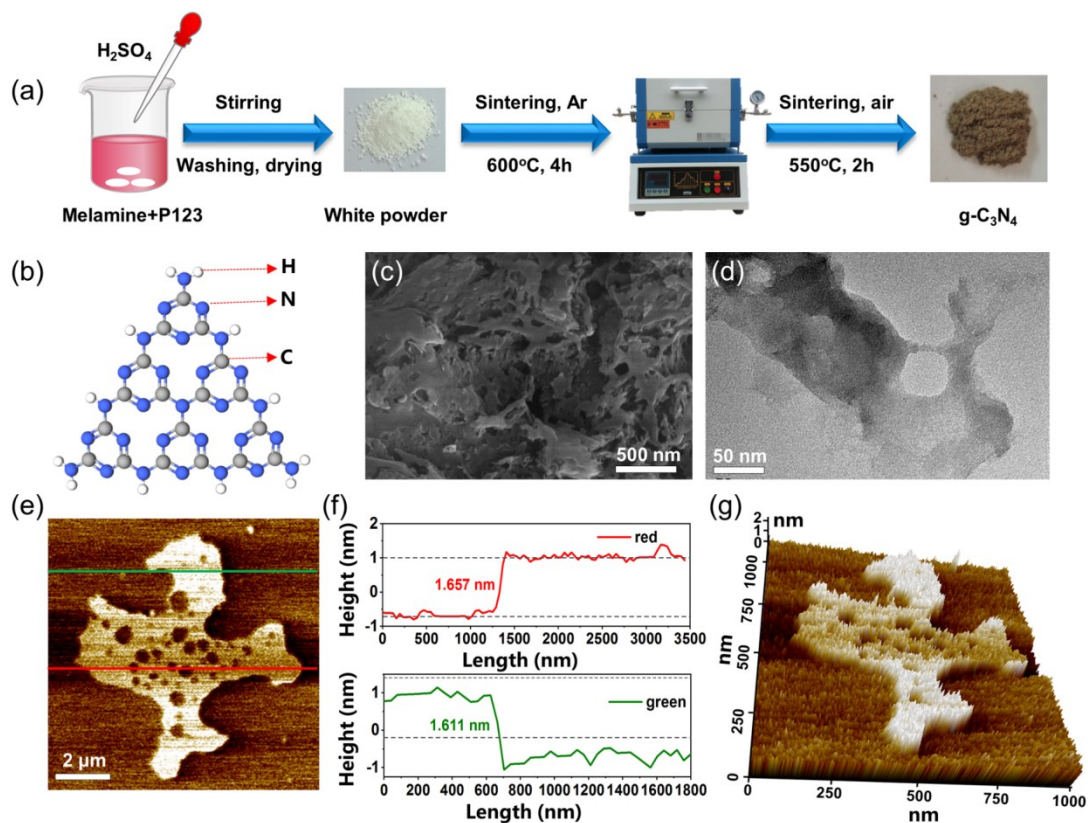


Figure S18. (a) Schematic diagram of preparation process of $g\text{-C}_3\text{N}_4$ nanosheets with melamine, surfactant P123 and H_2SO_4 as raw materials through solid-state sintering and thermal oxidation assisted exfoliation technique. (b) Schematic of molecular structure of $g\text{-C}_3\text{N}_4$. (c) SEM and (d) TEM images of as-synthesized 2D $g\text{-C}_3\text{N}_4$ nanosheets with porous structure. (e) 2D AFM image of as-synthesized $g\text{-C}_3\text{N}_4$ nanosheets on mica substrate. (f) The height profiles along the red and green lines in (e) image. (g) AFM image of 3D topography of as-synthesized $g\text{-C}_3\text{N}_4$ nanosheets, suggesting that the thickness of as-synthesized $g\text{-C}_3\text{N}_4$ nanosheets is uniform with porous structure.

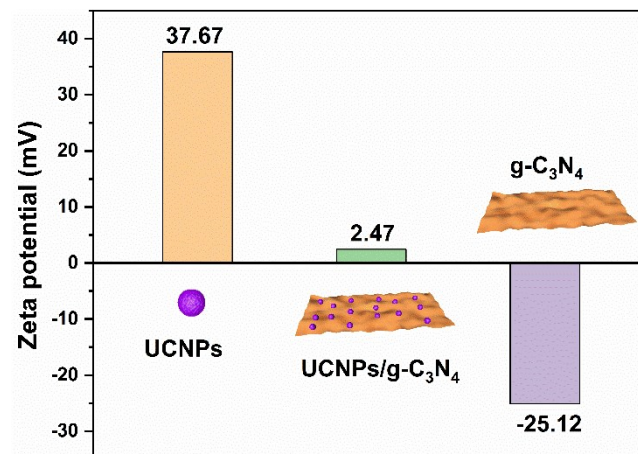


Figure S19. Zeta potentials of ligand-free LiYbF₄:Tm-LiYbF₄@LiYF₄ upconversion nanoparticles (UCNPs), g-C₃N₄ nanosheets and UCNPs/g-C₃N₄ nanocomposites in deionized water, indicating the UCNPs/g-C₃N₄ nanocomposites could be fabricated by electrostatic attraction between the positively charged UCNPs and the negatively charged g-C₃N₄.

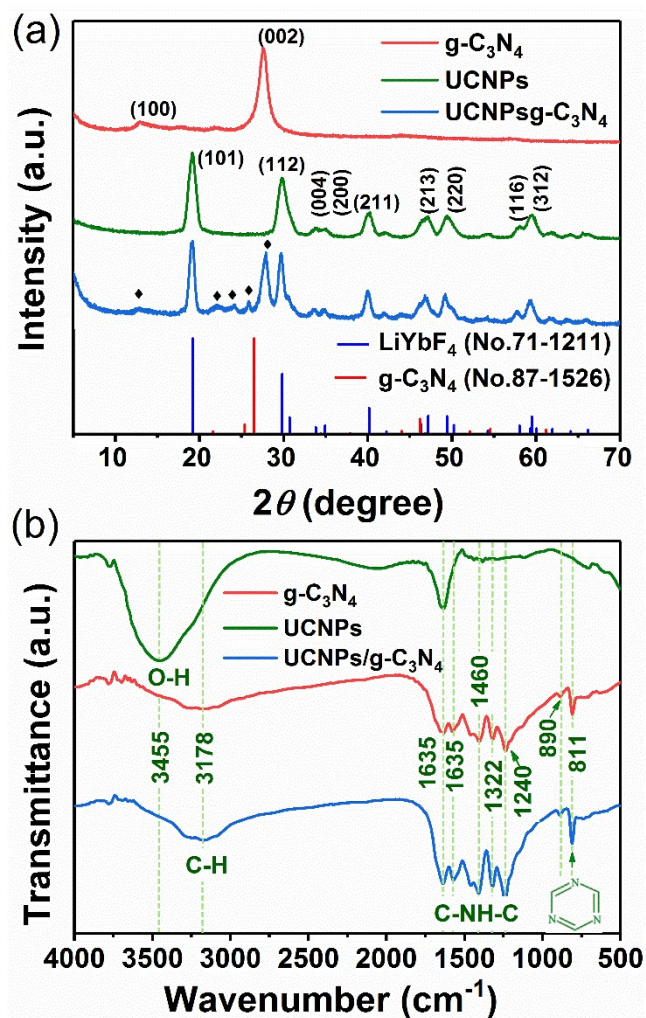


Figure S20. (a) XRD patterns of g-C₃N₄, UCNPs and UCNPs/g-C₃N₄ samples, respectively. Note that the standard JCPDS data for tetragonal-phased LiYbF₄ (PDF #71-1211) and graphite-phased g-C₃N₄ (PDF #87-1526) are also presented. The rhombus mark denotes the diffraction peaks of g-C₃N₄. (b) FT-IR spectra of UCNPs, g-C₃N₄ and UCNPs/g-C₃N₄ nanocomposites respectively.

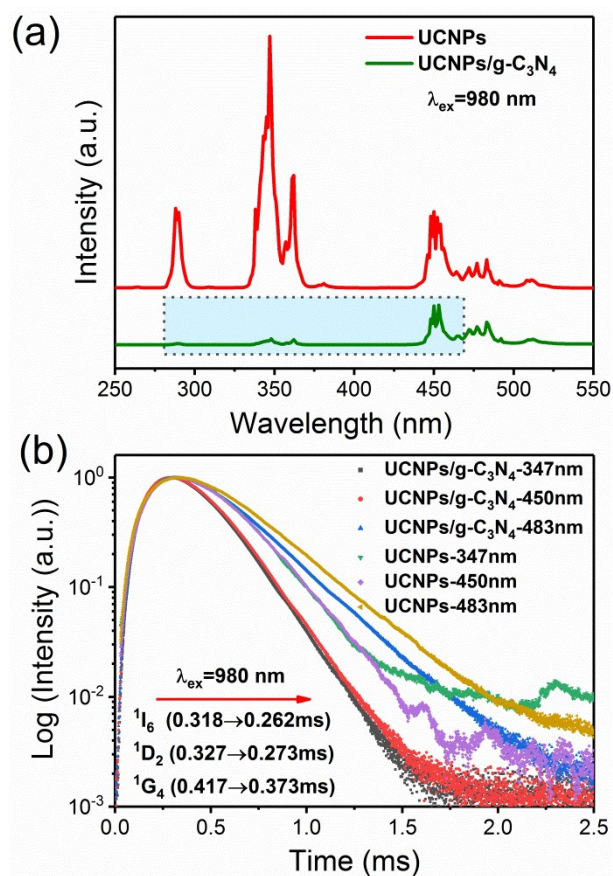


Figure S21. (a) Upconversion emission spectra of UCNPs and UCNPs/g-C₃N₄ nanocomposites under 980 nm excitation. (b) Decay curves of ¹I₆, ¹D₂ and ¹G₄ states of Tm³⁺ emissions in the UCNPs and UCNPs/g-C₃N₄ nanocomposites monitored at 347, 450, and 483 nm with a pulse laser at 980 nm, respectively.

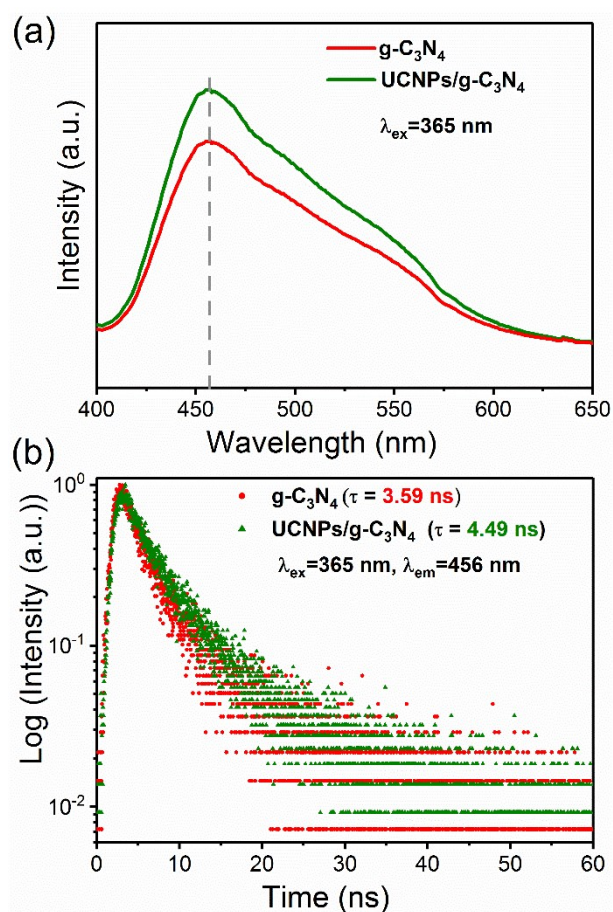


Figure S22. (a) Photoluminescence spectra of $\text{g-C}_3\text{N}_4$ nanosheets and UCNPs/ $\text{g-C}_3\text{N}_4$ nanocomposites under 365 nm excitation. (b) Decay curves of $\text{g-C}_3\text{N}_4$ nanosheets and UCNPs/ $\text{g-C}_3\text{N}_4$ nanocomposites monitored at 456 nm with a pulsed nanosecond hydrogen lamp at 365 nm.

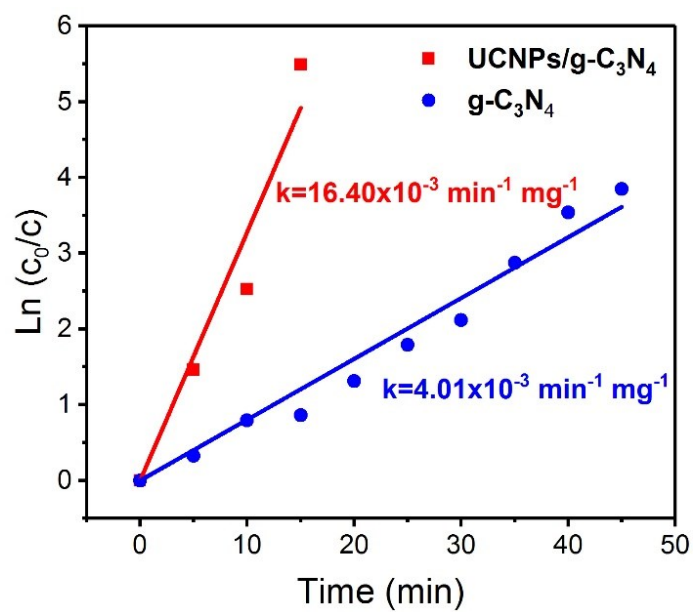


Figure S23. The plot of $\ln(c_0/c)$ vs reaction time for the photocatalytic degradation of MB over g-C₃N₄ nanosheets and UCNPs/g-C₃N₄ nanocomposites as photocatalysts under simulated solar light.

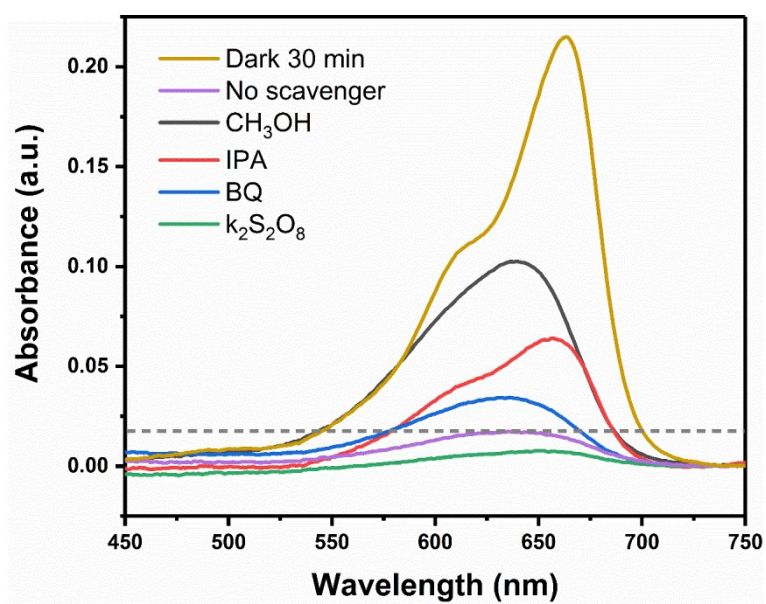


Figure S24. UV-vis absorption spectra of in the presence of four types of scavengers and UCNPs/g-C₃N₄ nanocomposites under the simulated solar light irradiation.

Table S1. Summarized the highest normalized reaction rate in some reported UCNPs-based nanocomposite for photocatalysis degradation.

Upconversion composite photocatalyst	Degradation system	Normalized highest reaction rate constant	Irradiation source	Ref.
LiYbF ₄ :Tm-LiYbF ₄ @LiYF ₄ /g-C ₃ N ₄	MB	16.40×10 ⁻³ min ⁻¹ mg ⁻¹	AM 1.5G	This Work
1 wt% Au-NaYF ₄ :Yb,Er,Tm/g-C ₃ N ₄ /Au	MO	0.874×10 ⁻³ min ⁻¹ mg ⁻¹	AM 1.5G	[1]
NaYF ₄ :Yb,Nd,Tm@NaYF ₄ :Yb,Nd@NaYF ₄ /g-C ₃ N ₄	MO	19×10 ⁻³ min ⁻¹	100 mW/cm ² Xe lamp	[2]
NaLuF ₄ :Gd,Yb,Tm@NaLuF ₄ :Gd,Yb@SiO ₂ @3wt%Ag/g-C ₃ N ₄	RhB	2×10 ⁻³ min ⁻¹ mg ⁻¹	300 W Xe lamp	[3]
NaYF ₄ :Yb,Tm@NaLuF ₄ @mSiO ₂ /Ag ₃ O ₄	RhB	14.13×10 ⁻³ min ⁻¹ mg ⁻¹	300 W Xe lamp	[4]
Er,Yb-(CaF ₂ @TiO ₂)	MO	2.64×10 ⁻³ min ⁻¹ L ⁻¹ mg ⁻¹	500 W Xe lamp	[5]
CaF ₂ :Er,Tm,Yb/BiVO ₄	MO	1.8×10 ⁻³ min ⁻¹ mg ⁻¹	1000 W HP mercury lamp	[6]

Note: Refs 1~6

- (1) Zhang, Q.; Deng, J.; Xu, Z.; Chaker, M.; Ma, D. High-Efficiency Broadband C₃N₄ Photocatalysts Synergistic Effects from Upconversion and Plasmons. *ACS Catal.* **2017**, 7 (9), 6225-6234.
- (2) Lee, S. Y.; Lee, G.; Jun, Y.-S.; Park, Y. I. Visible/near-infrared driven highly efficient photocatalyst based on upconversion nanoparticles/g-C₃N₄ nanocomposite. *Appl. Surf. Sci.* **2020**, 508.
- (3) Zhao, F.; Khaing, K. K.; Yin, D.; Liu, B.; Chen, T.; Wu, C.; Huang, K.; Deng, L.; Li, L. Large enhanced photocatalytic activity of g-C₃N₄ by fabrication of a

- nanocomposite with introducing upconversion nanocrystal and Ag nanoparticles. *RSC Adv.* **2018**, *8* (74), 42308-42321.
- (4) Chan, M. H.; Chen, C. W.; Lee, I. J.; Chan, Y. C.; Tu, D.; Hsiao, M.; Chen, C. H.; Chen, X.; Liu, R. S. Near-Infrared Light-Mediated Photodynamic Therapy Nanoplatform by the Electrostatic Assembly of Upconversion Nanoparticles with Graphitic Carbon Nitride Quantum Dots. *Inorg. Chem.* **2016**, *55* (20), 10267-10277.
- (5) Huang, S. Q.; Gu, L.; Miao, C.; Lou, Z. Y.; Zhu, N. W.; Yuan, H. P.; Shan, A. D. Near-infrared photocatalyst of Er³⁺/Yb³⁺ codoped (CaF₂@TiO₂) nanoparticles with active-core/active-shell structure. *J. Mater. Chem. A* **2013**, *1* (27), 7874-7879.
- (6) Huang, S.; Zhu, N.; Lou, Z.; Gu, L.; Miao, C.; Yuan, H.; Shan, A. Near-infrared photocatalysts of BiVO₄/CaF₂:Er³⁺, Tm³⁺, Yb³⁺ with enhanced upconversion properties. *Nanoscale* **2014**, *6* (3), 1362-1368.